Environmental Science & Technology

pubs.acs.org/est

Article

Porewater Lead Concentrations Limited by Particulate Organic Matter Coupled With Ephemeral Iron(III) and Sulfide Phases during Redox Cycles Within Contaminated Floodplain Soils

Christian Dewey, John R. Bargar, and Scott Fendorf*

Cite This: *Environ. Sci. Technol.* 2021, 55, 5878−5886

Read Online

ACCESS | Metrics & More | Article Recommendations | Supporting Information

ABSTRACT: Lead contamination in soils and sediments is a major threat to water quality. In surface and near-surface environments, Pb is not redox active; however, common Pb hosts, including Fe(III)-(hydr)oxides and sulfides, dissolve and precipitate as redox conditions change. Dissolution of Pb hosts may release Pb to porewater, leading to spikes in dissolved Pb concentrations and potential transport into surface or groundwater. Here, we examine the impacts of hydrologically coupled redox transitions on Pb partitioning in contaminated floodplain soils. We find that the affinity of Pb for particulate organic matter (POM), inclusive of mineral-associated organic matter, ensures that across redox transitions Pb is retained in the solid phase, despite host-phase (Fe(III)-(hydr)oxide and sulfide) dissolution. As seasonal hydrologic dynamics shift porewater redox conditions, Pb-bearing Fe(III)-(hydr)oxides (Pb-HFO) and sulfides (PbS) are dissolved and (re)precipitated. However, despite these shifts in redox conditions and associated host-phase transformations, Pb retention on POM, coupled with the formation of PbS and Pb-HFO, maintains dissolved Pb concentrations below 17 μg L^{-1}. Importantly, the predominance of Pb adsorbed on POM alongside low dissolved Pb concentrations indicates that Pb released from HFO and PbS is retained by POM. Thus, despite host-phase dissolution during redox transitions, partitioning of Pb to the aqueous phase is minimal and, therefore, transport of dissolved Pb is unlikely.

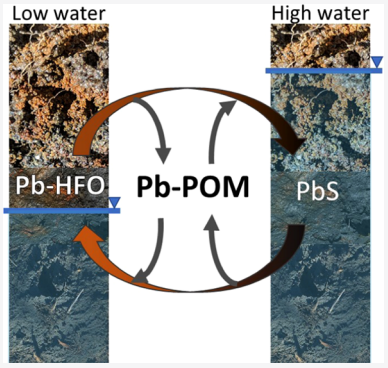

INTRODUCTION

Lead is a common contaminant in soils, presenting acute and chronic risks to freshwater quality. Assessing these risks requires an understanding of the processes that control Pb mobilization. Lead partitions strongly to solid phases under a range of biogeochemical conditions, generally limiting its mobility as a dissolved species. The low solubilities of common authigenic Pb minerals formed under anaerobic conditions (PbS, $PbCO_3$) and the high affinity of Pb^{2+} for Fe/Mn-(hydr)oxides formed in oxygenated environments maintain low concentrations of dissolved Pb across a range of redox conditions.[1−9] Lead also adsorbs strongly to particulate organic matter (POM, which we use to refer to all forms of organic matter within the solid phase), further limiting dissolved concentrations.[10]

However, transitions in redox conditions may alter the thermodynamic stability of Pb hosts, particularly sulfide and Fe/Mn-(hydr)oxide phases, resulting in their dissolution and the release of Pb to porewater. Indeed, the onset of anaerobic conditions and subsequent reductive dissolution of Fe(III)-(hydr)oxides (here collectively referred to as HFO) have been shown to release adsorbed Pb to the aqueous phase.[11] If the timescales of redox transitions and host-phase transformations are incommensurate, spikes in porewater Pb concentrations may occur.[11−13] Understanding the impacts of redox transitions on Pb partitioning is therefore needed to predict Pb behavior and the risks posed by Pb-contaminated soils to freshwater quality.

Here, we examine the effects of redox transitions on Pb partitioning by tracking aqueous Pb concentrations and solid-phase Pb speciation in riparian floodplain soils under shifting hydrologic conditions. Our study focuses on a mining-affected watershed near Crested Butte, CO. We hypothesized that seasonal redox transitions would dissolve Pb hosts, resulting in transient spikes in dissolved Pb. Our objectives were to resolve Pb speciation and partitioning across hydrologically controlled redox transitions and to determine the extent of Pb release during these transitions.

MATERIALS AND METHODS

Site Description. We examine floodplain soils from the Slate River watershed, near Crested Butte, CO. The watershed is a mountainous, high-elevation system (2700−4000 m ASL), in which seasonal snowmelt dominates hydrologic condi-

Received: December 2, 2020
Revised: April 12, 2021
Accepted: April 13, 2021
Published: April 26, 2021

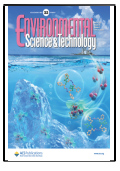

Downloaded via UNIV OF DENVER on November 22, 2022 at 03:43:04 (UTC).
See https://pubs.acs.org/sharingguidelines for options on how to legitimately share published articles.

ACS Publications

© 2021 American Chemical Society

https://doi.org/10.1021/acs.est.0c08162
Environ. Sci. Technol. 2021, 55, 5878−5886

tions.[14] Quaternary glacial soils of variable thickness are found throughout the watershed, underlain by Cretaceous to Tertiary sedimentary rocks intruded by porphyritic granitic stocks.[15,16] In general, the floodplains are overlain by Quaternary alluvium and colluvium. Our study site is located 100 m downstream from the confluence of Slate River and Oh-Be-Joyful Creek at 2726 m ASL. Oh-Be-Joyful Creek drains the Upper Redwell Basin, where historic mining activities targeted galena, among other ores.[15] The soil Pb contamination at our site is the result of transport of galena and weathering products from Redwell Basin, and its subsequent deposition in riparian alluvium, causing elevated soil Pb concentrations (Table S1).

Field Measurements and Sample Collection. Porewater and soil samples were collected at a location 15 m south of the Slate River (13S 324138.46 m E and 4308680.62 m N) (Figure S1). We refer to this location as OBJ-2. For porewater sampling, MacroRhizon porewater samplers (Rhizosphere Research Products, Wageningen, Netherlands; hereafter referred to as rhizons) with a 0.15 μm pore size were installed in October, 2017 at 50, 70, 90, 110, 130, and 150 cm below ground surface (bgs) in 7.5 cm boreholes. Two 9 cm rhizons were inserted vertically into the bottom of each borehole. Tygon tubing was run from the rhizon port to the ground surface. Each borehole was packed with excavated soil, with care to add soil in the reverse order to which it was removed.

Water and soil samples were collected from June 4 through October 26, 2018 at 2−4 week intervals. Porewater samples were collected by applying a vacuum with a 60 mL syringe to each rhizon for 30−60 min. Evacuated porewater was then dispensed into a 20 mL scintillation vial and a 40 mL amber glass vial for dissolved metal and TOC measurements, respectively. Samples for metal quantification were acidified with 0.5 M HCl. All water samples were stored at 4 °C until laboratory analyses (performed within 3 months of sampling). Porewater pH was measured in the field.

Soil samples were collected with a 7.5 cm bucket auger at the depths of the rhizons. At each depth, 20−30 g of soil was removed from the auger with a stainless-steel spatula and packed into a glass serum vial, which was immediately capped with a butyl stopper. A hand pump was used to evacuate the vial headspace. The sealed vials were frozen in the field and stored at −18 °C until transfer to an anaerobic chamber (95% N_2, 5% H_2 atmosphere; Coy Laboratory Products, Inc., Grass Lake, MI), where the vials were opened and recapped. The recapped vials were stored at −18 °C. On each sampling date, soil samples were collected within 1 m of the rhizon cluster.

Depth to groundwater was tracked hourly from December 1, 2017 through December 13, 2018. A pressure transducer (Onset Computer Corporation, Bourne, MA) was installed at OBJ-2 for this purpose. The transducer was suspended on a galvanized steel cable to a depth of 130 cm bgs in a 2 m open well. Absolute pressure was logged at 1 h intervals. The measurements were converted to groundwater depth using barometric pressure measurements from the East River floodplain (10.5 km distance; 2723 m ASL), which were logged at the same frequency with an identical transducer.

Elemental Concentrations. Dissolved Pb was measured on a Thermo Scientific XSERIES 2 quadrupole inductively coupled plasma mass spectrometer (Thermo Fisher Scientific, Waltham, MA). Dissolved Fe and S were measured on a Thermo Scientific ICAP 6300 Duo View inductively coupled plasma optical emission spectrometer with a solid-state CID detector (Thermo Fisher Scientific). Samples were diluted in 2% HNO_3 prior to analyses. Concentrations of solid-phase metals were measured by X-ray fluorescence (XRF) with a SPECTRO Xepos HE XRF spectrometer (SPECTRO Analytical Instruments GmbH, Kleve, Germany). Soils were dried and ground in an anaerobic chamber before XRF analysis. Total dissolved organic carbon (DOC) was measured on a Shimadzu TOC-V total carbon analyzer (Shimadzu Scientific Instruments, Kyoto, Japan.) Solid-phase carbon was measured on a CN Elemental Analyzer (Carlo Erba, Cornaredo, Italy).

X-ray Absorption Spectroscopy. Lead L_3-edge extended X-ray absorption fine structure (EXAFS) spectra were collected at the Stanford Synchrotron Radiation Lightsource (SSRL) at beamlines 7-3, 9-3, and 11-2 (between 3 and 9 months after collection). For collection of spectra, wet soils were ground to a fine paste and pressed into aluminum sample holders, which were sealed with Kapton tape. The samples were stored in an anaerobic chamber (95% N_2, 5% H_2 atmosphere) until transfer to a liquid helium cryostat at the beamline. Mineral specimens were obtained from Mineralogical Research Company (San Jose, CA) for collection of X-ray absorption (XAS) standards. Their purity was verified with X-ray diffraction. Pb adsorbed on goethite (Pb-Gt) was synthesized in the lab according to Schwertmann and Cornell[17] and Bargar et al.[18] The Pb-POM spectrum used in this study was collected by Morin et al.[19]

For all Pb EXAFS measurements, incident X-ray energy was controlled with an LN_2-cooled Si(220) double monochromator in the φ = 90° configuration. To eliminate higher-order harmonics, the monochromator at 7-3 was detuned 30% at 13.4 keV, while an in-hutch Rh harmonic rejection mirror with the cutoff set to 15 keV was used at beamlines 9-3 and 11-2. Measurements were performed at 10 K. Fluorescence spectra of the soils and the Pb-Gt standard were collected using a 30-element (beamline 7-3) or 100-element (beamlines 9-3 and 11-2) Ge detector array (Canberra, Meriden, CT). Transmission spectra were collected for the mineral standards at beamline 7-3 using an N_2-filled ionization chamber. An in-line Pb foil was used for energy calibration at all beamlines. Calibration and alignment of the spectra were performed in SIXPack.[20] Spectra were normalized and background-subtracted in Athena.[21,22] Linear combination fitting (LCF) was performed in Athena on k^3-weighted spectra between k = 2 Å^{-1} and k = 10.5 Å^{-1}. The following standards were used in the LCF analysis: Pb-Gt, Pb adsorbed on particulate organic matter (Pb-POM), galena, cerussite, anglesite, and pyromorphite. Shell-by-shell analyses were performed in SIXPack using FEFF 8.4 to generate scattering paths.[20,22]

Elemental maps were collected by microscale X-ray fluorescence (μXRF) mapping at SSRL beamline 2-3. Soils were dried and embedded in degassed epoxy (EpoTek 301) in an anaerobic chamber (5% H_2, 95% N_2), and petrographic thin sections were prepared (Spectrum Petrographics, Vancouver, WA). The μXRF maps were collected in air. Thin sections were stored anaerobically before and after analysis. Incident X-ray energy was controlled with a water-cooled Si(111) double-crystal monochromator. A spot size of 2 × 2 μm^2 was used. A Fe-metal foil (K-edge at 7112 eV) was used for energy calibration. Incident energy on the sample was set at 13 100 eV. μXRF maps were collected at a 10 μm step size (with a dwell time of 25−100 ms/point). X-ray fluorescence yield was measured using a 4-element Vortex Silicon Drift Detector

https://doi.org/10.1021/acs.est.0c08162
Environ. Sci. Technol. 2021, 55, 5878−5886

(Hitachi, Schaumburg, IL). The software package SMAK was used for processing and analysis of the elemental maps.[23]

Sulfur K-edge X-ray absorption near edge structure (XANES) spectra were collected at SSRL beamline 4-3. Soils were dried, finely ground, and loaded into aluminum sample holders, which were sealed with a polyethylene film and S-free Kapton tape. Samples were stored in an anaerobic chamber (95% N_2, 5% H_2) until transfer to the anaerobic He atmosphere in the beamline sample box. Incident X-ray energy was controlled with a water-cooled Si(111) double monochromator in the $\varphi = 90°$ configuration. Fluorescence spectra were collected using a 4-element Vortex Silicon Drift Detector. Measurements were performed at room temperature with a dwell time of 1 s. We did not observe indications of beam damage during the measurements. The thiosulfate pre-edge feature at 2472.0 eV was used for energy calibration. The spectra were calibrated, normalized, background-subtracted, and fit using Athena.[21,22]

RESULTS

Floodplain Hydrologic Conditions. Groundwater levels at OBJ-2 varying seasonally, reflecting seasonal discharge dynamics of the Slate River and the construction of a beaver dam. Water levels peak at 32 cm below ground surface (bgs) in late May, corresponding with maximum snowmelt across the watershed (Figure 1).[14] Water levels decline to 105 cm bgs by early August, after which they rise until early October, reaching 55 cm bgs (Figure 1). The late-season rise in water levels was due to construction of a beaver dam on the Slate River 20 m downstream from OBJ-2 (Figure S2).

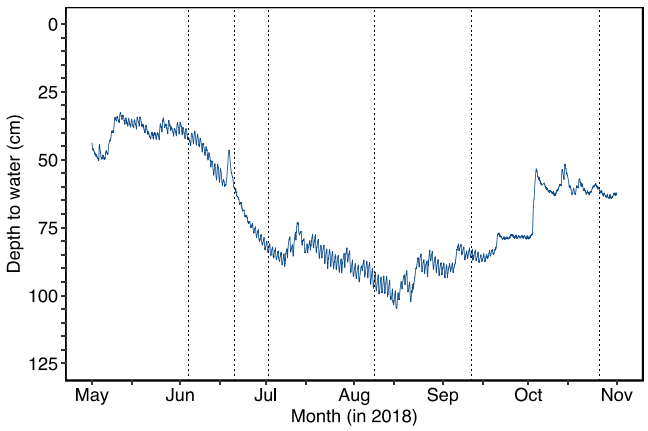

Figure 1. Water table position (cm below ground surface) at site OBJ-2 from May 1 through November 1, 2018. Vertical dashed lines indicate porewater and solid-phase sampling dates (June 4, June 20, July 2, August 8, September 11, and October 26). Minor tick marks are placed at the 15th of each month. High water in May corresponds to the peak river stage due to snowmelt. The increase in the water table position from mid-August to mid-October was driven by construction of a beaver dam in the Slate River immediately downstream from the Oh-Be-Joyful floodplain.

Porewater Chemistry. Throughout the majority of the sampling campaign, dissolved Pb concentrations were consistently below 72.5 nM (15 $\mu g\ L^{-1}$), the action level established by the US EPA Lead and Copper Rule for primary drinking water (Figure 2; Table S4).[24] Starting in August, Pb concentrations generally increase at all depths as water levels rise. The increase is pronounced at 50 and 70 cm (Figure 2). Cascade filtration (0.60, 0.45, 0.10, and 0.02 μm) on porewater from 130 cm collected on August 8 suggests that the vast majority (>96%) of aqueous Pb occurs passes through 0.02 μm filter pores (Table S2). Porewater pH, which was measured in June and October at 50 and 130 cm, ranged from 6.0 to 7.0 (Table S3).

The concentrations of total dissolved S, Fe, and Mn vary with depth, with S and Fe changing sharply between 90 and 110 cm and Mn between 70 and 90 cm. In general, total dissolved S gradually increases from 50 to 90 cm, from 37.5 to 172 μM, and sharply decreases below 90 cm to less than 31.3 μM (Figure 2; Table S4). In contrast, total dissolved Fe increases slightly from 50 to 90 cm, from less than 17.9 to 39.3−82.1 μM, then sharply increases from 90 to 130 cm, to 207−348 μM, before slightly decreasing from 130 to 150 cm, to 127−191 μM (Figure 2). Total dissolved Mn exhibits more variability than Fe and S at 50 cm, with concentrations ranging from 0.120 to 7.88 μM. From 70 to 90 cm, Mn concentrations increase, from 0.220−2.23 to 4.09−6.07 μM (Figure 2). From 90 to 130 cm, Mn concentrations do not change appreciably with depth, ranging from 4.65 to 4.88 μM, before dropping from 130 to 150 cm, to 1.00−2.61 μM (Figure 2). Cascade filtration suggests that 39.6% of measured Fe, 59.8% of measured S, and 41.8% of measured Mn pass through 0.02 μm filter pores (Table S2).

Porewater Fe, Mn, and S concentrations change with seasonal hydrologic conditions throughout the soil profile. In general, porewater Fe and Mn first increase with falling water levels (from June 4 to June 20) and then decrease as water levels decline to a minimum in mid-August, while porewater S behaves oppositely. Iron concentrations above 90 cm, while low, are highly variable (Figures 2 and S3). At 90 cm, Fe concentrations increase from June 4 to July 2 by 60.2% but decrease from July 2 to August 8 by 42.3% as the water table falls to its minimum (Figure S3). Like Fe, porewater Mn above 90 cm is highly variable, with concentrations at 50 cm increasing by 67.6% from June 4 to June 20 and decreasing by 165% from June 20 to August 8. At 70 cm depth, Mn concentrations increase 18.1% from June 4 to June 20 and decrease by 108% from June 20 to August 8 (Figure S4). As the water table falls from its seasonal high in early June to its minimum in mid-August, total S concentrations increase at 50 and 70 cm depths by 74.4 and 31.9%, respectively (Figure S5). At 90 cm, Mn concentrations increase by 18.5% as water levels fall between June 4 and August 8 (Figure S4). Porewater Fe behaves similarly at 110 cm depth, increasing by 15.7% over this period, while S and Mn concentrations decrease by 41.1 and 5.40%, respectively (Figures S4 and S5). At 130 cm depth, porewater Fe and Mn generally decrease between June and August, by 16.3 and 8.50%, respectively. At 150 cm depth, S and Mn increase by 53.8 and 9.90% between June 4 and August 8, respectively, and Fe decreases by 11.0% (Figures S3−S5).

Porewater chemistry also changes as water levels rise after construction of the beaver dam. Below 110 cm depth, the dam appears to cause a reversal of the S, Fe, and Mn concentration trends observed with the decline of water levels between June and August. As water levels rise, porewater Fe and Mn generally increase, while S decreases. At 130 and 150 cm, porewater S decreases (−10.6 and −7.60%) between August 8 and October 26, while Fe concentrations increase (26.3 and 29.4%) (Figures S3 and S5). Manganese concentrations decrease from August 8 to September 11 (68.1%) but increase

https://doi.org/10.1021/acs.est.0c08162
Environ. Sci. Technol. 2021, 55, 5878−5886

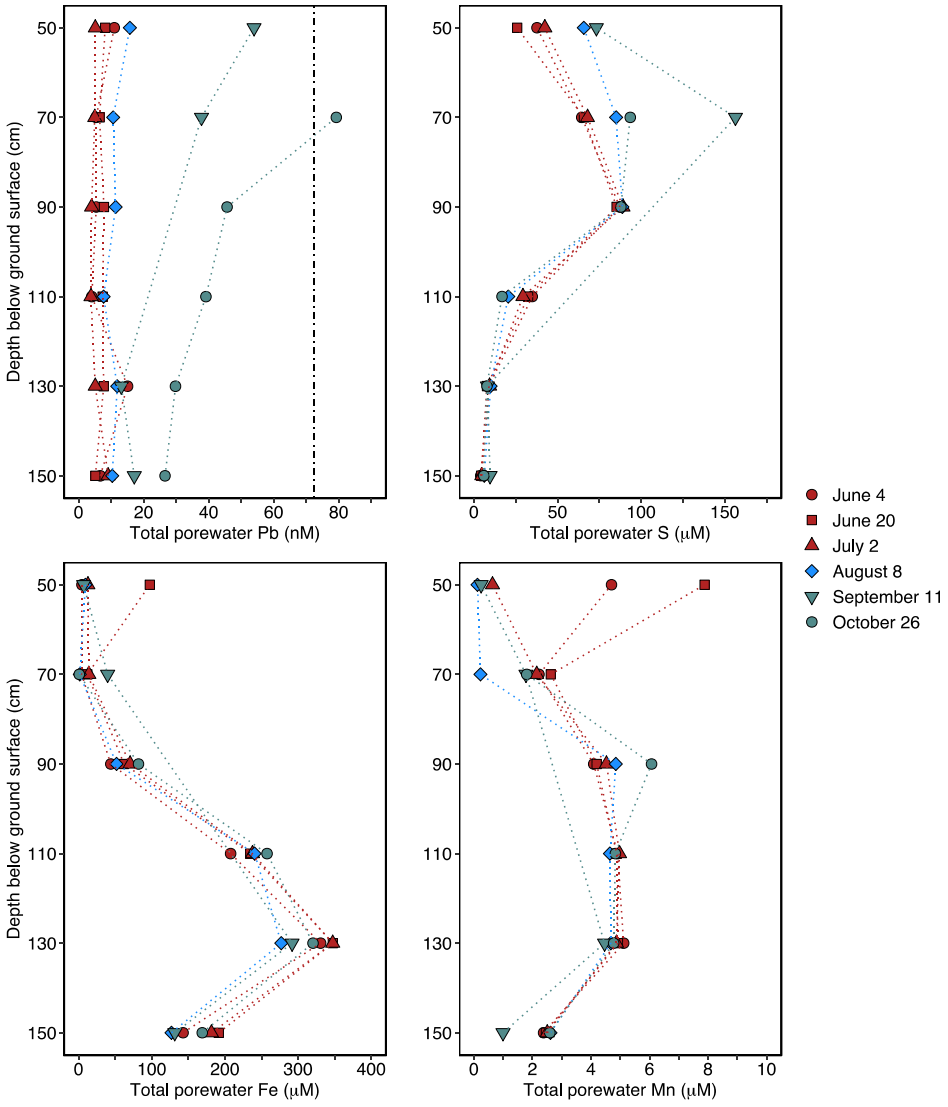

Figure 2. Depth-resolved total porewater concentrations of Pb (top left), Fe (bottom left), S (top right), and Mn (bottom right) from June 4 through October 26, 2018. The vertical dashed line indicates the EPA regulatory limit for dissolved Pb.

from September 11 to October 26 (67.1%) (Figure S4). At 110 cm depth, Mn and Fe concentrations increase following construction of the dam (3.80 and 8.20%), while S concentrations decrease (10.8%) (Figures S3−S5). At and above a depth of 90 cm, Fe increases from August 8 to September 11 (by up to 926%) and then decreases from September 11 to October 26 (by up to −943%) (Figure S3). From August 8 to October 26, Mn increases at and above 90 cm (29.9% at 90 cm; 71.0% at 70 cm), while total S decreases slightly at 90 cm (−1.10%) and increases at 50 and 70 cm depths (13.0%) (Figures S3 and S5).

Total DOC concentrations generally increase with depth. At 90 cm and above, concentrations ranged from 0.157 to 0.269 mM (Table S5). Below a depth of 90 cm, concentrations ranged from 0.225 to 0.752 mM, with the highest concentrations occurring at 110 and 130 cm bgs (Table S5). Cascade filtration indicates that 57.0% of measured DOC passes through 0.02 μm filter pores (Table S2). Solid soil C varied between 0.770 and 5.18% and generally increased with depth (Table S6).

Solid-Phase S Speciation. Sulfur K-edge XANES spectra were collected on soils from each depth and all sampling dates. Linear combination fitting (LCF) of the spectra was performed with the following standards: $CaSO_4$, dodecyl sulfate; sulfonic acid; methionine; L-cystine; elemental sulfur; and mackinawite. In the fits, we take $CaSO_4$ to represent inorganic sulfate, dodecyl sulfate to represent organosulfates, and methionine and L-cystine to represent reduced organic S species (e.g., S-bearing amino acids). The predominant solid S species are elemental S, organic reduced S, and organosulfates. In general, the proportion of reduced S (elemental S, reduced organic S, and mackinawite) increases with depth, while the proportion of oxidized S (organosulfates) decreases with depth (Figure S6). As with total dissolved Fe and S concentrations, a sharp transition in S speciation occurs between 90 and 110 cm depths (Figure S6). Above depths of 110 cm, 50−75% of solid-phase S occurs as organic and inorganic sulfate species (±5%; this uncertainty applies to all subsequent components); 20−30% of solid-phase S occurs as reduced organic S species; and 10−30% occurs as elemental S (Figure S6). Below 90 cm, organosulfates comprise 30−50% of total S at 110 cm and 5−25% at 130 and 150 cm depths (Figure S6). No inorganic sulfate is detected below 90 cm. The proportion of elemental S below 90 cm increases as the proportion of organosulfates

https://doi.org/10.1021/acs.est.0c08162
Environ. Sci. Technol. 2021, 55, 5878−5886

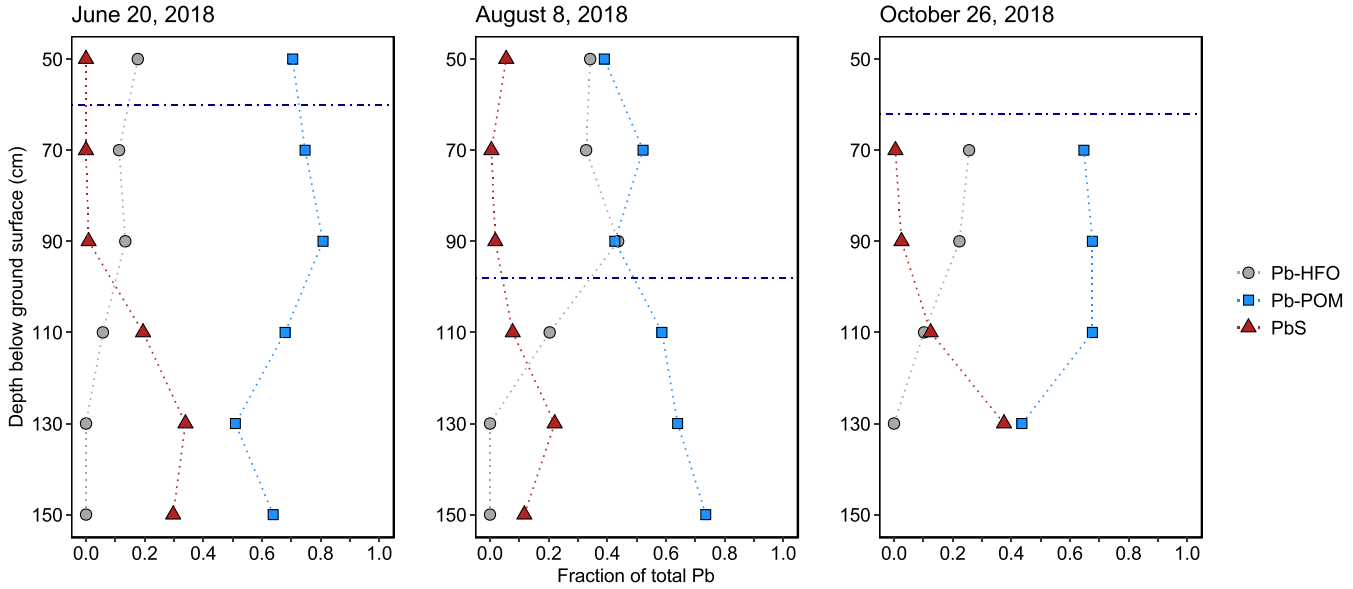

Figure 3. Linear combination fitting (LCF) results of Pb L_3-edge EXAFS spectra of sediments collected on June 20, August 8, and October 26, 2018. The dotted horizontal line indicates the water table position at the time of sampling. The LCF was performed with the following standards: cerussite, galena (PbS), anglesite, pyromorphite, Pb-POM, and Pb-Gt (Pb-HFO). For clarity, only the Pb-POM, PbS, and Pb-HFO results are shown here, as the other standards comprised less than 10% of the overall fit. Full LCF results appear in the Supporting Information (Tables S13–S15; Figures S13–S15).

decreases. Elemental S accounts for 10–65% of total S, with the greatest proportions generally detected at 150 cm depth (Figure S6). Mackinawite is also detected below 110 cm, ranging from 6 to 30% of total S, with maximums at a depth of 150 cm (Figure S6). The proportion of methionine generally increases below 90 cm, while the proportion of L-cystine decreases (Figure S6). The S XANES spectra and fits are shown in Figures S7–S12, and fitting results are tabulated in Tables S7–S12.

Solid-Phase Pb Concentrations and Speciation. Solid-phase Pb concentrations range from 137 to 340 mg kg^{-1}, with an average of 209 mg kg^{-1} and a standard deviation of 57 mg kg^{-1} (Table S1). In general, Pb concentrations decrease with depth (Table S1). We used Pb L_3-edge EXAFS spectroscopy and μXRF mapping to characterize Pb speciation in the soils. The Pb EXAFS measurements were performed on soils collected on June 20, August 8, and October 26. μXRF maps were collected on soils from 40 and 130 cm bgs collected on October 16, 2017. The Pb EXAFS spectra and μXRF maps reveal that Pb occurs in three predominant phases: Pb adsorbed to particulate organic matter (Pb-POM); poorly crystalline PbS, and Pb adsorbed to Fe(III)-(hydr)oxides (Pb-HFO). Due to nearly identical local coordination environments for Pb adsorbed on HFO (ferrihydrite, goethite, and hematite), we do not distinguish between the Fe(III) phases in our analysis of the Pb EXAFS and refer to them collectively as HFO.

Linear combination fitting of the Pb EXAFS spectra indicates that solid-phase Pb occurs predominantly as Pb-POM, with lesser amounts of Pb-HFO and PbS. Overall, the proportions of Pb-HFO and PbS decrease and increase (respectively) with depth, while Pb-POM makes up the balance (Figure 3). Similar to solid-phase S speciation and total dissolved Fe and S concentrations, a sharp transition in Pb speciation occurs between 90 and 110 cm depths (Figure 3). Pb-HFO accounts for 11–44% of solid Pb above 90 cm and 0–20% below 90 cm (±10%; applies to all components), while PbS accounts for <5% of solid Pb above 90 cm and 8–34% below 90 cm depth (Figure 3; Tables S11–S13). Across the profile, Pb-POM comprises 39–75% of Pb (Figure 3; Tables S13–S15). The LCF also indicates that pyromorphite, anglesite, and cerussite are below the detection limit of EXAFS analysis and, if present, comprise less than 10% of total Pb (Figure 3; Tables S13–S15). The Pb EXAFS spectra and LCFs are shown in Figures S13–S15.

Speciation of solid-phase Pb changes throughout the sampling campaign. From June 20 to August 8, the proportion of Pb-HFO increases above 90 cm depth, concurrent with a decrease in the proportion of Pb-POM (Figure 3). Below 90 cm, the proportion of PbS decreases from June to August, while the proportion of Pb-POM increases (Figure 3). From August 8 to October 26, the proportion of Pb-HFO decreases above 90 cm, and the proportion of Pb-POM increases (Figure 3). Below a depth of 90 cm, the proportion of PbS increases and the proportion of Pb-POM decreases (Figure 3).

Shell-by-shell analysis of Pb EXAFS spectra supports the conclusion that Pb-POM predominates along the profile. We analyzed spectra from the 50 and 130 cm depth samples collected on (respectively) June 20 and October 26, treating these samples as representative of Pb speciation above and below 90 cm, as well as the Pb-Gt, PbS, and Pb-POM standards (Figure S16; Table S16). In fitting the spectra, it was necessary to include a first-shell Pb–O pair at a distance consistent with Pb-POM but, crucially, incompatible with the Pb–O distance in Pb-HFO. For the 50 cm sample, the first-shell Pb–O distance was fit at 2.34 (±0.01) Å (Table S16), a distance 0.06 Å longer than the Pb–O distance measured for Pb-Gt and 0.04 Å longer than the maximum Pb–O distance reported in the literature for Pb-HFO (2.30 Å).[5] Given the narrow distribution of Pb–O distances for Pb-HFO (Figure 4) and the sensitivity of Pb L_3-edge EXAFS to first-shell distances (0.01 Å), the Pb–O distance measured in the 50 cm sample indicates that a Pb phase other than Pb-HFO predominates. This phase is likely Pb-POM, as the Pb–O distance is within

https://doi.org/10.1021/acs.est.0c08162
Environ. Sci. Technol. 2021, 55, 5878–5886

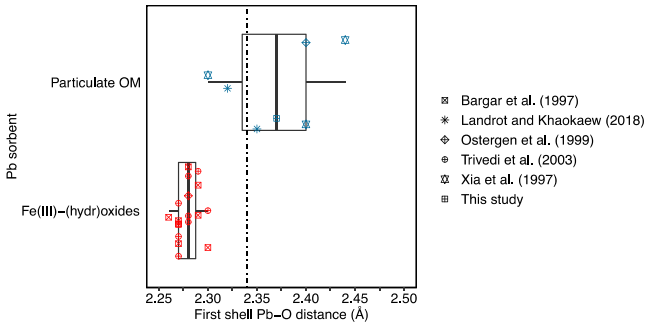

Figure 4. Box and whisker plots showing distributions of published first-shell Pb−O distances (as measured by Pb L_3-edge EXAFS) for Pb adsorbed on particulate organic matter (blue) and Fe(III)-(hydr)oxides (red). A range of organic matter and Fe(III)-(hydr)oxides (goethite, ferrihydrite, and hematite) are represented. The vertical dashed line indicates the first-shell Pb−O distance measured for the sample collected from 50 cm bgs on June 20, 2018.

the range of published Pb−O distances for Pb-POM (2.30−2.45 Å) (Figure 4).[25]

Although the first-shell distance rules out Pb-HFO as the predominant Pb phase, analysis of the second shell reveals a mixture of Pb-POM and Pb-HFO. A second-shell Fe backscatterer is apparent in the Fourier transform of the EXAFS spectrum (Figure S16). The distance derived for this Pb−Fe pair is 3.32 Å (Table S16), consistent with Pb−Fe distances for Pb adsorbed in a bidentate edge-sharing configuration with FeO_6 octahedra in HFO.[5,18,25,26] This confirms the presence of Pb-HFO. Thus, while Pb-POM dominates speciation, Pb-HFO is present in detectable amounts.

The Debye−Waller factor (DW) and the coordination number (CN) for the first Pb−O shell of the 50 cm sample further support a predominant Pb-POM phase and minor Pb-HFO phase. The first-shell DW, which is twice that derived for Pb-Gt, suggests a mixture of Pb phases with Pb−O distances distributed around 2.34 Å, consistent with a mixture of Pb-POM and Pb-HFO.[9,18] Moreover, the EXAFS-derived CN for the first oxygen shell (2.98) is high relative to the first-shell CN derived for Pb-HFO.[9,18,27] Attenuation of CNs in the EXAFS-fitted Pb−O shell is commonly reported for Pb EXAFS spectra of Pb-HFO.[9,18,27] The attenuation results from a distribution of distances in the first oxygen shell, which produce destructive interference and suppressed amplitude in the EXAFS spectrum, yielding a low first-shell CN.[9] Destructive interference may also be occurring in the 50 cm sample, but the larger CN indicates an arrangement of first-shell O atoms that differs from that of Pb-HFO, likely reflecting a disordered first shell of organic O-ligands.

Altogether, analyses of the first and second shells indicate that Pb-POM is the dominant Pb phase above 90 cm and that a smaller pool of Pb-HFO is also present. Pyromorphite, anglesite, and cerussite, if present, occur in concentrations too low to make a significant contribution to the local coordination environment.

The EXAFS spectrum of the sample from 130 cm is dominated by a local structure consistent with PbS. Fitting Pb−S and Pb−Pb pairs at 2.92 and 4.16 Å, distances characteristic of PbS,[28] accounts for the majority of the EXAFS amplitude and structure (Figure S16; Table S16). However, the EXAFS-derived coordination numbers for the S and Pb shells (2.07 and 5.03, respectively) are less than half of the expected values for crystalline PbS (6 and 12, for S and Pb, respectively) (Table S16). This indicates that PbS likely occurs as a poorly crystalline phase and, further, points to a second predominant Pb phase. Given that the Pb−S and Pb−Pb pairs fit the majority of the EXAFS features, it is unlikely that a phase with local order and heavy backscatterers accounts for the missing amplitude; inclusion of such a phase would be necessary to capture the high-k EXAFS spectral features. A phase with a weak second-shell backscatterer thus likely dominates. Furthermore, the phase likely exhibits a highly disordered first shell: a narrow distribution of first-shell distances would produce a distinct frequency in the EXAFS and a prominent peak in the Fourier transform. This would rule out Pb-HFO as the predominant phase, given the narrow distribution of first-shell Pb−O distances for Pb-HFO (Figure 4). A predominant Pb-POM phase is, by contrast, consistent with the analysis. A highly disordered first O shell in Pb-POM (2.30−2.45 Å) (Figure 4) would diminish the EXAFS amplitude arising from PbS without necessarily producing a strong peak in the Fourier transform.

To further constrain Pb speciation, μXRF maps were collected on soils from 40 and 130 cm bgs (Figure S17). The μXRF maps and Pb−Fe correlations suggest that PbS and Pb-HFO occur in deep and shallow soils, respectively. In the sediment from 40 cm bgs, the majority of Pb is distributed throughout the particles and is correlated with the presence of Fe (R^2 = 0.34) (Figure S17), which may reflect coprecipitated POM and HFO with associated Pb. A small pool of Pb occurs as 20−30 μm particles in which Fe is not present (PbS was not detected by EXAFS in the shallow soils, ruling out its contribution). In 130 cm depth soil, the majority of Pb occurs as 20−60 μm particles in which Fe is not present. Based on the Pb EXAFS analysis, these grains are likely PbS. There is also a sizeable amount of Pb that is distributed throughout the grains and associated with Fe (R^2 = 0.17), indicating the presence of Pb-HFO and Pb-OM at depth.[29−32]

DISCUSSION

Redox Conditions Coupled to Seasonal Hydrology. Throughout the study period, there is a distinct transition in redox conditions in the Slate River floodplain between the depths of 90 and 110 cm. The transition is apparent in the porewater Fe, Mn, and S profiles, as well as the solid-phase S speciation. Above 90 cm, aerobic and Mn-reducing conditions appear to dominate, while below 110 cm, Fe and sulfate-reducing conditions dominate. However, seasonal changes in hydrology appear to alter porewater redox conditions across the profile, particularly at depths above 90 cm.

Transient saturation above 90 cm appears to cause a seasonally oscillating redox transition from aerobic to anaerobic conditions. High water levels in May and June result in saturation of the soil above 90 cm depth (Figure 1), leading to limited oxygen supply and concomitant reduction of Fe- and Mn-(hydr)oxides. Iron and Mn reduction during high water is revealed with increased Fe and Mn concentrations at these depths. The decline in Fe and Mn concentrations indicates a return to aerobic conditions at low water. At 50 cm depth, Mn concentrations increase from June 4 to June 20 by 67.6% and then progressively decline into August, when they are 97.4% less than on June 4 (Figures 1, 2, and S4). Iron concentrations also spike on June 20, increasing by over 20-fold, and then decline into August (Figures 2 and S3). Dissolved S concentrations oppose Fe and Mn, declining by

https://doi.org/10.1021/acs.est.0c08162
Environ. Sci. Technol. 2021, 55, 5878−5886

31.4% on June 20 and then increasing 74.4% into August (Figures 2 and S5). At 70 cm depth, changes in Mn, Fe, and S concentrations are consistent with the changes at 50 cm depth, though they are smaller in magnitude. Consistent with thermodynamic predictions, Mn-reducing conditions develop before Fe-reducing conditions, but the fact that measurable Fe was observed above 90 cm indicates that Fe reduction is occurring (likely within aggregates).

With the construction of the beaver dam in mid-August, water levels rise at the site, driving the soil above 90 cm into reducing conditions. This is apparent in the rebound of Mn concentrations at 70 cm depth in September and October (Figure S3). Iron concentrations also increase at this depth in September, indicating ongoing Fe reduction despite relatively low Fe concentrations. With the apparent return to anaerobic conditions after construction of the beaver dam, dissolved S concentrations increase, indicating that the beaver-induced water table rise does not lead to sulfate-reducing conditions.

Redox conditions below 90 cm also respond to changes in hydrology, despite these horizons being continuously saturated. Throughout the study period, dissolved Fe concentrations reveal a transition to Fe-reducing conditions between 90 and 110 cm (Figure 2). The increase in dissolved Fe is mirrored by a decrease in dissolved S, indicating that sulfate reduction occurs alongside Fe reduction at these depths. Yet, as the water table falls, Fe and Mn concentrations generally decline, revealing decreased Fe-reducing activity, despite continuous saturation. At 110 and 130 cm depth, Mn concentrations decrease as the water table falls from June 4 to August 8. Following construction of the beaver dam and rise in the water table, Mn concentrations at these depths increase by up to 5% (Figure S4). Below 110 cm, Fe concentrations decrease with the fall of the water table between June and August and then rebound as water levels rise after construction of the beaver dam, while dissolved S concentrations behave oppositely (Figures S3 and S5). Throughout the study period, sulfate reduction occurs below 110 cm depth, revealed by the appearance of FeS (mackinawite) and the predominance of S^0, which is commonly produced by reduction of Fe(III) by dissolved sulfide and oxidation of FeS by dissolved oxygen (Figure S6).[33,34] The peak in Fe and Mn concentrations at 130 cm indicates that below this depth, sulfate reduction replaces Fe reduction as the predominant microbial metabolism, perhaps due to the accumulation of Fe(II).

Dynamic Repartitioning of Pb. The temporal and spatial redox transitions resulting from seasonal hydrology drive dissolution of Pb host phases. Yet throughout and across these redox transitions, dissolved Pb concentrations remain near or below the US EPA drinking water standard (15 $\mu g\ L^{-1}$). As the water table falls from June 4 through August 8, the proportion of Pb-HFO above 110 cm increases 19−22%, while the proportion of Pb-POM decreases by the same amount, revealing dynamic repartitioning of Pb between these phases in the upper soil horizons (Figure 3). The decrease in the water table likely drives the formation of poorly crystalline Fe(III)-(hydr)oxides, with a high affinity for Pb. As the water table rises with the construction of the beaver dam between August and October, reduction of the poorly crystalline Fe phases occurs, driving repartitioning of Pb onto POM (Figure 3). Despite the transfer of Pb, and therefore Pb release, between POM and HFO, dissolved Pb concentrations remain below 82.1 nM (17 $\mu g\ L^{-1}$) (Figure 2). Lead released during Fe cycling in these soils appears to repartition sufficiently rapidly to limit increases in dissolved concentrations, at least over the frequency of our sampling. The affinity of Pb for organic matter[19,25] appears to result in POM buffering-dissolved Pb concentrations throughout seasonal redox transitions.

Below 90 cm depth, seasonal variation in Pb speciation also appears coupled to hydrologic-redox transitions. As water levels decline between June and August, the proportion of PbS decreases, while the proportions of Pb-POM and (at 110 cm) Pb-HFO increase (Figure 3). This likely reflects the formation of poorly crystalline PbS under reducing conditions in June and July. The PbS phase then dissolves as the soils drain between June and August, leading to the transfer of Pb to POM and HFO. With the rise in the water table from August to October, the proportion of PbS increases while the proportion of Pb-OM decreases (Figure 3). Nonetheless, dissolved Pb concentrations remain below 48.3 nM (10 $\mu g\ L^{-1}$) throughout these transitions. Lead released to porewater via dissolution of PbS and HFO likely adsorbs to POM. As in the upper soil horizons, POM thus appears to play a critical role in limiting dissolved Pb concentrations during redox transitions.

■ ENVIRONMENTAL IMPLICATIONS

The affinity of Pb for sulfide phases, HFO, and functional groups on POM, which reflects its stability in a range of coordination environments, limits porewater Pb concentrations during redox transitions. Although changes in redox conditions dissolve Pb hosts and release associated Pb, adsorption on POM and freshly formed mineral hosts (iron phases upon drainage and sulfide phases upon water saturation) maintain low porewater Pb concentrations. POM may be an important sink for released Pb if formation of a fresh mineral host phase occurs more slowly than Pb release. Our findings suggest that exports of dissolved Pb from floodplain soils are minimal, even with active dissolution of Pb hosts, provided there is sufficient POM and S to ensure solid-phase partitioning of Pb during hydrologically driven redox cycles. Particulate OM imparts a particularly important role in limiting dissolved Pb concentrations through seasonal changes in hydrology and associated redox conditions.

■ ASSOCIATED CONTENT

Supporting Information

The Supporting Information is available free of charge at https://pubs.acs.org/doi/10.1021/acs.est.0c08162.

Soil XRF results; map of the study site; picture of the beaver dam; cascade filtration results; description of the cascade filtration procedure; porewater pH measurements; tabulated porewater Fe, S, Mn, and Pb concentrations; percent change in aqueous Fe, Mn, and S; DOC concentrations; soil %C content; S K-edge XANES LCF summary plots; S K-edge XANES spectra; tabulated S K-edge XANES LCF results; Pb L_3-edge EXAFS spectra; tabulated Pb L_3-edge EXAFS LCF results; Pb L_3-edge EXAFS shell-by-shell fits; tabulated results of Pb L_3-edge EXAFS shell-by-shell fit; and micro-XRF Fe−Pb elemental maps and correlation plots (PDF)

https://doi.org/10.1021/acs.est.0c08162
Environ. Sci. Technol. 2021, 55, 5878−5886

AUTHOR INFORMATION

Corresponding Author

Scott Fendorf − *Department of Earth System Science, Stanford University, Stanford, California 94305, United States;* orcid.org/0000-0002-9177-1809; Email: fendorf@stanford.edu

Authors

Christian Dewey − *Department of Earth System Science, Stanford University, Stanford, California 94305, United States;* orcid.org/0000-0003-1954-8298

John R. Bargar − *SLAC National Accelerator Laboratory, Menlo Park, California 94025, United States;* orcid.org/0000-0001-9303-4901

Complete contact information is available at: https://pubs.acs.org/10.1021/acs.est.0c08162

Notes

The authors declare no competing financial interest.

ACKNOWLEDGMENTS

This research was supported by the SLAC Groundwater Quality SFA program of the U.S. Department of Energy, Office of Biological and Environmental Research, Subsurface Biogeochemistry Program (SBR), and by the SBR Project Award Number DE-SC0016544. Use of the Stanford Synchrotron Radiation Lightsource, SLAC National Accelerator Laboratory, is supported by the U.S. Department of Energy, Office of Science, Office of Basic Energy Sciences, under contract No. DE-AC0276SF00515. Field and logistical support was provided by the Rocky Mountain Biological Laboratory (RMBL) in Gothic, CO. We thank Juan Lezama Pacheco (Stanford University) and Guangchao Li (Stanford University) for their technical assistance. We also thank Gordon Brown (Stanford University) for supplying the Pb L_3-edge EXAFS spectrum of Pb-POM. Finally, we thank Ken Williams (Lawrence Berkeley National Laboratory) and Jennie Reithel (Rocky Mountain Biological Laboratory) for field and logistical support.

REFERENCES

(1) Kumpiene, J.; Lagerkvist, A.; Maurice, C. Stabilization of As, Cr, Cu, Pb and Zn in Soil Using Amendments − A Review. *Waste Manage.* **2008**, *28*, 215−225.

(2) Bradham, K. D.; Diamond, G. L.; Nelson, C. M.; Noerpel, M.; Scheckel, K. G.; Elek, B.; Chaney, R. L.; Ma, Q.; Thomas, D. J. Long-Term in Situ Reduction in Soil Lead Bioavailability Measured in a Mouse Model. *Environ. Sci. Technol.* **2018**, *52*, 13908−13913.

(3) Matocha, C. J.; Elzinga, E. J.; Sparks, D. L. Reactivity of Pb(II) at the Mn(III,IV) (Oxyhydr)Oxide−Water Interface. *Environ. Sci. Technol.* **2001**, *35*, 2967−2972.

(4) Strawn, D. G.; Scheidegger, A. M.; Sparks, D. L. Kinetics and Mechanisms of Pb(II) Sorption and Desorption at the Aluminum Oxide−Water Interface. *Environ. Sci. Technol.* **1998**, *32*, 2596−2601.

(5) Trivedi, P.; Dyer, J. A.; Sparks, D. L. Lead Sorption onto Ferrihydrite. 1. A Macroscopic and Spectroscopic Assessment. *Environ. Sci. Technol.* **2003**, *37*, 908−914.

(6) Dyer, J. A.; Trivedi, P.; Scrivner, N. C.; Sparks, D. L. Lead Sorption onto Ferrihydrite. 2. Surface Complexation Modeling. *Environ. Sci. Technol.* **2003**, *37*, 915−922.

(7) Vulava, V. M.; Seaman, J. C. Mobilization of Lead from Highly Weathered Porous Material by Extracting Agents. *Environ. Sci. Technol.* **2000**, *34*, 4828−4834.

(8) Müller, B.; Sigg, L. Adsorption of Lead(II) on the Goethite Surface: Voltammetric Evaluation of Surface Complexation Parameters. *J. Colloid Interface Sci.* **1992**, *148*, 517−532.

(9) Bargar, J. R.; Brown, G. E.; Parks, G. A. Surface Complexation of Pb(II) at Oxide-Water Interfaces: I. XAFS and Bond-Valence Determination of Mononuclear and Polynuclear Pb(II) Sorption Products on Aluminum Oxides. *Geochim. Cosmochim. Acta* **1997**, *61*, 2617−2637.

(10) Xia, K.; Bleam, W.; Helmke, P. A. Studies of the Nature of Cu2+ and Pb2+ Binding Sites in Soil Humic Substances Using X-Ray Absorption Spectroscopy. *Geochim. Cosmochim. Acta* **1997**, *61*, 2211−2221.

(11) Weber, F.-A.; Voegelin, A.; Kretzschmar, R. Multi-Metal Contaminant Dynamics in Temporarily Flooded Soil under Sulfate Limitation. *Geochim. Cosmochim. Acta* **2009**, *73*, 5513−5527.

(12) Hansel, C. M.; Benner, S. G.; Nico, P.; Fendorf, S. Structural Constraints of Ferric (Hydr)Oxides on Dissimilatory Iron Reduction and the Fate of Fe(II). *Geochim. Cosmochim. Acta* **2004**, *68*, 3217−3229.

(13) Higgins, S. R.; Hamers, R. J. Chemical Dissolution of the Galena(001) Surface Observed Using Electrochemical Scanning Tunneling Microscopy. *Geochim. Cosmochim. Acta* **1996**, *60*, 3067−3073.

(14) Winnick, M. J.; Carroll, R. W. H.; Williams, K. H.; Maxwell, R. M.; Dong, W.; Maher, K. Snowmelt Controls on Concentration-Discharge Relationships and the Balance of Oxidative and Acid-Base Weathering Fluxes in an Alpine Catchment, East River, Colorado. *Water Resour. Res.* **2017**, *53*, 2507−2523.

(15) Kimball, B. A.; Runkel, R. L.; Wanty, R. B.; Verplanck, P. L. Reactive Solute-Transport Simulation of Pre-Mining Metal Concentrations in Mine-Impacted Catchments: Redwell Basin, Colorado, USA. *Chem. Geol.* **2010**, *269*, 124−136.

(16) Gaskill, D. L.; Godwin, L. H.; Mutschler, F. E. Geologic Map of the Oh-Be-Joyful Quadrangle, Gunnison County, Colorado. *U.S. Geological Survey Geologic Quadrangle Map CQ-578*, 1967.

(17) Schwertmann, U.; Cornell, R. M. *Iron Oxides in the Laboratary*; Wiley-VCH Verlag GmbH: Weinheim, Germany, 2000.

(18) Bargar, J. R.; Brown, G. E.; Parks, G. A. Surface Complexation of Pb(II) at Oxide-Water Interfaces: II. XAFS and Bond-Valence Determination of Mononuclear Pb(II) Sorption Products and Surface Functional Groups on Iron Oxides. *Geochim. Cosmochim. Acta* **1997**, *61*, 2639−2652.

(19) Morin, G.; Ostergren, J. D.; Juillot, F.; Ildefonse, P.; Calas, G.; Brown, G. E. XAFS Determination of the Chemical Form of Lead in Smelter-Contaminated Soils and Mine Tailings; Importance of Adsorption Processes. *Am. Mineral.* **1999**, *84*, 420−434.

(20) Webb, S. M. SIXpack: A Graphical User Interface for XAS Analysis Using IFEFFIT. *Phys. Scr.* **2005**, *T115*, 1011−1014.

(21) Ravel, B.; Newville, M. ATHENA, ARTEMIS, HEPHAESTUS: Data Analysis for X-Ray Absorption Spectroscopy Using IFEFFIT. *J. Synchrotron Radiat.* **2005**, *12*, 537−541.

(22) Ankudinov, A. L.; Ravel, B.; Rehr, J. J.; Conradson, S. D. Real-Space Multiple-Scattering Calculation and Interpretation of x-Ray Absorption near-Edge Structure. *Phys. Rev. B* **1998**, *58*, 7565−7576.

(23) Webb, S. M.; McNulty, I.; Eyberger, C.; Lai, B. The MicroAnalysis Toolkit: X-Ray Fluorescence Image Processing Software. *AIP Conf. Proc.* **2011**, 196−199.

(24) U.S. Environmental Protection Agency. Maximum Contaminant Level Goals Nad National Primary Drinking Water Regulations for Lead and Copper; Final Rule. *Fed. Regist.* **1991**, *56*, No. 26460.

(25) Ostergren, J. D.; Brown, G. E.; Parks, G. A.; Tingle, T. N. Quantitative Speciation of Lead in Selected Mine Tailings from Leadville, CO. *Environ. Sci. Technol.* **1999**, *33*, 1627−1636.

(26) Scheinost, A. C.; Abend, S.; Pandya, K. I.; Sparks, D. L. Kinetic Controls on Cu and Pb Sorption by Ferrihydrite. *Environ. Sci. Technol.* **2001**, *35*, 1090−1096.

(27) Bargar, J.; Brown, G.; Parks, G. Surface Complexation of Pb(II) at Oxide-Water Interfaces: III. XAFS Determination of Pb(II) and

Pb(II)-Chloro Adsorption Complexes on Goethite and Alumina. *Geochim. Cosmochim. Acta* **1998**, *62*, 193−207.
(28) Lebedev, A.; Sluchinskaya, I.; Munro, I. EXAFS Study of PbS-SnS Solid Solution. *J. Synchrotron Radiat.* **2001**, *8*, 800−802.
(29) Kaiser, K.; Guggenberger, G. The Role of DOM Sorption to Mineral Surfaces in the Preservation of Organic Matter in Soils. *Org. Geochem.* **2000**, *31*, 711−725.
(30) Mikutta, R.; Mikutta, C.; Kalbitz, K.; Scheel, T.; Kaiser, K.; Jahn, R. Biodegradation of Forest Floor Organic Matter Bound to Minerals via Different Binding Mechanisms. *Geochim. Cosmochim. Acta* **2007**, *71*, 2569−2590.
(31) Wagai, R.; Mayer, L. M. Sorptive Stabilization of Organic Matter in Soils by Hydrous Iron Oxides. *Geochim. Cosmochim. Acta* **2007**, *71*, 25−35.
(32) Lalonde, K.; Mucci, A.; Ouellet, A.; Gélinas, Y. Preservation of Organic Matter in Sediments Promoted by Iron. *Nature* **2012**, *483*, 198−200.
(33) Noël, V.; Boye, K.; Kukkadapu, R. K.; Bone, S.; Lezama Pacheco, J. S.; Cardarelli, E.; Janot, N.; Fendorf, S.; Williams, K. H.; Bargar, J. R. Understanding Controls on Redox Processes in Floodplain Sediments of the Upper Colorado River Basin. *Sci. Total Environ.* **2017**, *603−604*, 663−675.
(34) Burton, E. D.; Bush, R. T.; Sullivan, L. A. Acid-Volatile Sulfide Oxidation in Coastal Flood Plain Drains: Iron−Sulfur Cycling and Effects on Water Quality. *Environ. Sci. Technol.* **2006**, *40*, 1217−1222.

https://doi.org/10.1021/acs.est.0c08162
Environ. Sci. Technol. 2021, 55, 5878−5886